


Terahertz dynamic multiband perfect absorber with a digital coding graphene-diamond metasurface

Shaowei Zhang,¹ Feng Wen^{1,*}, Muhua Zhai,¹ Zheng Li,¹ Huapeng Ye², Hengxi Zhang,³ Yangxin Gu,¹ Yang Lei,¹ Wei Wang,¹ Yanpeng Zhang,¹ and Hongxing Wang^{1,†}

¹Key Laboratory for Physical Electronics and Devices of the Ministry of Education & School of Science & Shaanxi Key Laboratory of Information Photonic Technique & Institute of Wide Bandgap Semiconductors & Key Laboratory of Multifunctional Materials and Structures, Ministry of Education, School of Electronic Science and Engineering, Xi'an Jiaotong University, Xi'an 710049, China

²SCNU-TUE Joint Lab of Device Integrated Responsive Materials (DIRM), National Center for International Research on Green Optoelectronics, South China Normal University, Guangzhou 510006, China

³Armament Science and Technology College, Xi'an Technological University, Xi'an 710021, China

 (Received 16 January 2024; revised 30 April 2024; accepted 6 June 2024; published 2 August 2024)

The monolayer graphene-based terahertz (THz) perfect absorber has made significant progress in switchable devices with diverse functionalities. However, existing methods for achieving switchability rely on either multilayered metasurface with complex configurations or complicated patterned metasurfaces. A switchable absorber that switches between n -band and m -band modes (n , m correspond to the number of resonance peaks) using tunable materials is also interesting but has not yet been mentioned. Here, a dynamically switchable multiband perfect absorber with a digital coding graphene metasurface is proposed and demonstrated. By integrating multiple metasurface units with different Fermi levels into a newly generated period, we realize a multiband perfect absorber with a rather simple and straightforward configuration composed of a patterned metasurface. Through introducing a digital coding metasurface into the perfect absorber, we use the digital signals via FPGA (field programmable gate array) to convert n -band into m -band absorption modes. Moreover, the results reveal that the THz perfect absorber, possessing great impedance matching with the free space, has excellent angle tolerance and robustness. Such a perfect absorber offers a flexible tool for selecting THz channels and may pave the way for sixth-generation communication.

DOI: [10.1103/PhysRevApplied.22.024004](https://doi.org/10.1103/PhysRevApplied.22.024004)

I. INTRODUCTION

The terahertz (THz) waveband, located between microwave and far infrared, has attracted increasing attention due to various potential applications, including prospective sixth-generation (6G) communication [1], remote sensing [2], nondestructive medical detection [3–5], and quantum optics [6–8]. Unfortunately, natural materials that are highly responsive to THz waves are rather limited, rendering the development of THz devices slow and leaving a “THz gap.” The emergence of the metamaterial, which is usually defined as a three-dimensional periodically arranged artificial structure with a subwavelength-feature size, breaks this situation because it can be designed to primarily respond to THz waves [9]. The metamaterial is gradually being replaced by a metasurface consisting of a two-dimensional thin-film structure [10], which is easier

to process and fabricate. Initially, the electromagnetic loss of the metal material becomes the main challenge in building left-handed materials. However, the loss turns out to be an advantage in the field of perfect absorbers. Some efforts have been devoted to investigating metal-based metasurface perfect absorbers [11–13], but these absorbers are not dynamically tunable and have limited functions owing to the untuned characteristics of the metal.

To overcome the bottleneck of nonadjustability, previously, researchers tended to focus on the active metasurface composed of a tunable material, such as graphene [14,15], liquid crystals [16], vanadium dioxide (VO₂) [17–19], and doped silicon [20]. Among these materials, graphene attracts more attention, because its electron mobility and Fermi level can be tuned by manipulating the external electrostatic field [21], magnetic field [22], optical pump [23], and temperature, thus leading to excellent tunability. Substantial studies on graphene-based single-band [24], dual-band [25,26], multiband [27–29], and broadband [30,31] tunable perfect absorbers have been

*Contact author: fengwen@mail.xjtu.edu.cn

†Contact author: hxwangcn@mail.xjtu.edu.cn

performed in the past decade. For example, Sun *et al.* [26] proposed a graphene-based dual-band independently tunable perfect absorber consisting of double-stacked graphene layers. A quad-band polarization-insensitive perfect absorber based on a bilayer graphene metasurface was demonstrated by Zamzam *et al.* [32]. Moreover, Darvishi Bahlooli *et al.* [29] developed a multiband (five narrow bands) monolayer-graphene perfect absorber with an extremely intricate design. An intelligent device with switchable and tunable multifunctionalities is also significantly attractive. The phase-change material VO₂ has a natural advantage in realizing multifunctional devices due to the rapid modulation performance between the metal phase and insulator phase [33]. The metal-insulator transition can be triggered by thermal heating, electrical bias, and optical excitation. Utilizing the tunability of both graphene and VO₂, adjustable broadband [17], switchable wideband-narrowband [18], and dual-broadband [34] perfect absorbers have been reported. Furthermore, a switchable multifunctional THz metasurface [35] exhibiting excellent performances of quad-band perfect absorption and an antireflection coating is also demonstrated. However, previous studies relied on either a complex multilayer structure or an intricately patterned metasurface unit to achieve multiple resonance modes, which necessitate intricate fabrication processes and precise lithography techniques. Additionally, once the device has been built, the absorption mode (the magnitude of the resonance peak) cannot be changed. Dynamically switchable perfect absorbers working with the *n*-band and *m*-band modes have not been studied. Therefore, it is noteworthy to explore a type of flexible and switchable perfect absorber of several absorption modes according to realistic demands.

Here, we propose and demonstrate a universal strategy for achieving a multiband THz adjustable graphene metasurface perfect absorber by adjusting the graphene

Fermi level. Meanwhile, the perfect absorber adopting a digital coding metasurface controlled by FPGA (field programmable gate array) expediently realizes the conversion of absorption modes from *n*-band to *m*-band with higher freedom and flexibility. The absorber employs a typical sandwiched subwavelength configuration consisting of a simple graphene rectangle strip pattern and a single-layered metasurface. Through optimizing the geometric parameters, the results reveal good impedance matching to reach perfect absorption. Eventually, the device can obtain a satisfactory angle tolerance. The absorber proposed here may have good application prospects in THz filtering [36] and high-performance sensors [37,38].

II. MODELING AND PARAMETERS

The proposed THz switchable perfect absorber with a graphene digital coding metasurface is illustrated in Fig. 1(a1), where the left and right parts are the microcontroller FPGA and graphene perfect absorber, respectively. Three-bit digital output ports (bit 0, bit 1, and bit 2) of FPGA are utilized to manipulate the Fermi levels, E_{F1} , E_{F2} , and E_{F3} , respectively, of the graphene strips. Every bit has two states [0 (1) state]: the 0 (1) state of bit 0 is 0 eV (0.088 eV), bit 1 is 0 eV (0.118 eV), and bit 2 is 0 eV (0.148 eV). Specifically, each digital bit line leaves the FPGA and passes through the digital-to-analog converter (DAC), which can convert the digital logic signal into an analog voltage. The two lines at the end of the DACs are the upper and lower lines, which are the analog voltage and ground lines, respectively. The upper analog voltage line with modulated voltage is connected to the electrodes on the insulation layer, and then separated into multiple gate-voltage lines to manipulate the Fermi level of the graphene strips. The lower line is connected to the bottom metal, offering a system voltage reference.

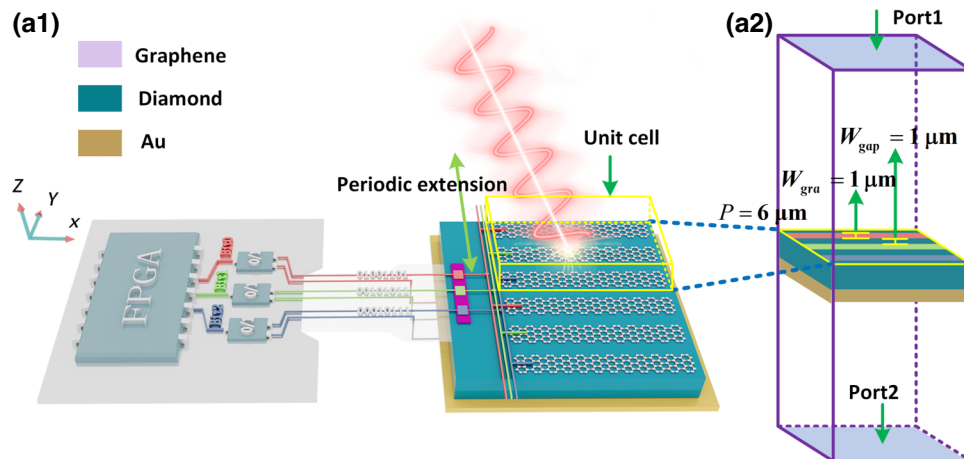


FIG. 1. (a1) Three-dimensional schematic of the proposed THz metasurface perfect absorber with digital coding metasurface. (a2) Sketch of a metasurface unit cell.

The right THz perfect absorber of Fig. 1(a1) consists of three layers: the monolayer-graphene metasurface, diamond dielectric, and the bottom metal. To pave the way for future experimental implementation, the metal electrode, the metal-graphene contact, and the graphene-diamond contact should be considered. First, due to the skin effect, the metal electrode (such as Au) needs to be designed to be smaller and thinner to reduce reflection efficiency and improve absorption efficiency. Second, the ubiquitous Fermi-level pinning effect caused by the metal-graphene contact can degrade the performance of electronic devices and increase the device's energy consumption, which can be reduced by a type of van der Waals contact achieved by using a selenium buffer layer between Au and graphene [39]. Eventually, the use of hydrogen-terminated diamond (111) is due to the negligible band-gap opening [40,41] at the Dirac point of graphene when the diamond is in contact with graphene, and the graphene-on-diamond structure can be experimentally achieved through graphitization [42,43] of the surface of diamond (111). The metal-graphene and graphene-diamond contacts will cause the Fermi level of graphene to shift [40,44]. Nevertheless, for our THz multiband perfect absorber scheme, the effective and dynamic modulation of the relative value of the Fermi level is more important than that of its absolute value, so we can apply an appropriate voltage to balance the influence of the two types of shift effect [45].

Here, we use COMSOL Multiphysics with the electromagnetic wave frequency-domain module for numerical calculations. In Fig. 1(a1), only two unit cells for the THz multiband perfect absorber are displayed; one cell is modeled in Fig. 1(a2). Port1 and Port2 are set to excite and absorb THz waves, respectively. We apply the periodic boundary conditions in the x - z plane to present a periodic distribution in the y direction and set a perfect electric conductor in the y - z plane. The diamond used here has excellent optical properties, with transmittance ranging from deep ultraviolet to far infrared, and even to microwave bands [46], except for the small intrinsic absorption of 4–6 μm . Meanwhile, the real and imaginary parts of the refractive index of diamond hardly change from 2.7 to 4.5 THz. Furthermore, the corresponding studies have shown that, when the temperature increases from 50 to 925 K, the refractive index of diamond only changes by about 0.009 [47]. Therefore, diamond is used as the dielectric material with a refractive index [46] of 2.41 and thermal conductivity [48] of 20 W/(cm K). The bottom metal (Au) is used as a perfect reflector with a conductivity [14] of $\sigma_{\text{gold}} = 4.7 \times 10^7$ S/m and a thickness of $d_{\text{gold}} = 0.3$ μm , which is larger than the skin depth of the THz wave. Therefore, in the calculation, the interface between diamond and the bottom metal is set as a perfect electric conductor to ensure that the transmittance is zero. In addition, the bottom metal and graphene strips can form a Fabry-Perot (FP) cavity to further improve the

absorptance rate of the THz multiband perfect absorber. The three graphene stripes in the unit cell are established as the transition boundary condition, where its surface conductivity takes following form [49]:

$$\begin{aligned} \sigma_{\text{gra}} &= \sigma_{\text{gra}}^{\text{intra}} + \sigma_{\text{gra}}^{\text{inter}}, \quad (1) \\ \sigma_{\text{gra}}^{\text{intra}} &= \frac{-i}{\omega + i\tau^{-1}} \frac{e^2}{\pi \hbar^2} \int_0^\infty E \left[\frac{\partial f(E)}{\partial E} - \frac{\partial f(-E)}{\partial E} \right] dE, \quad (2) \\ \sigma_{\text{gra}}^{\text{inter}} &= i(\omega + i\tau^{-1}) \frac{e^2}{\pi \hbar^2} \int_0^\infty \frac{f(-E) - f(E)}{(\omega + i/\tau)^2 - 4(E/\hbar)^2} dE, \quad (3) \end{aligned}$$

where ω represents the angular frequency of incident light; τ is the relaxation time of graphene (estimated by the maximum mobility of graphene) and is set as 3.28 ps [14]. The total surface conductivity of Eq. (1) is composed of the intraband conductivity of Eq. (2) and the interband conductivity of Eq. (3). The Fermi-Dirac distribution, $f(E)$, is $1/[e^{(E-E_F)/(k_B T)} + 1]$, where k_B is the Boltzmann constant, the Fermi level is defined as $E_F \approx (\pi \hbar^2 v_F^2 n)^{0.5}$, \hbar is the Planck constant, and v_F is the Fermi velocity equal to 10^6 m/s. n represents the carrier concentration in the conduction band, which is determined by the applied gate voltage through $n = \epsilon_r \epsilon_0 V_0 / e h_d$. ϵ_r is the relative dielectric constant of the dielectric material between the metal and graphene (such as the ion gel, with $\epsilon_r = 2.56$) [35], which is used to reduce the pinning effect of the Fermi level. ϵ_0 is the vacuum permittivity; e is the electron charge; and V_0 and h_d are the gate voltage and thickness of the dielectric layer, respectively.

In the near-infrared and visible regimes, the interband transition dominates the surface conductivity. Nevertheless, for the THz band, surface conductivity is mainly decided by the intraband transition, and the interband transition is suppressed due to Pauli blocking. Based on these considerations, the total surface conductivity can be approximated as the Drude model:

$$\sigma_{\text{gra}} = \frac{e^2 E_F}{\pi \hbar^2} \frac{i}{(\omega + i\tau^{-1})}. \quad (4)$$

Figures 2(a1) and 2(a2) show the real part and imaginary part of the conductivity, respectively. The relative permittivity of graphene is derived based on solving the Maxwell equations and takes the form $\epsilon_{\text{gra}} = 1 + i\sigma/(\omega \Delta \epsilon_0)$. Its imaginary part, proportional to the real part of conductivity, characterizes the losses, whereas the real part is proportional to the imaginary part of conductivity with the opposite sign in value. The real part and imaginary part of relative permittivity are depicted in Figs. 2(b1) and 2(b2). Here, Δ is the thickness of monolayer graphene, and extensive measurements of that have recently been

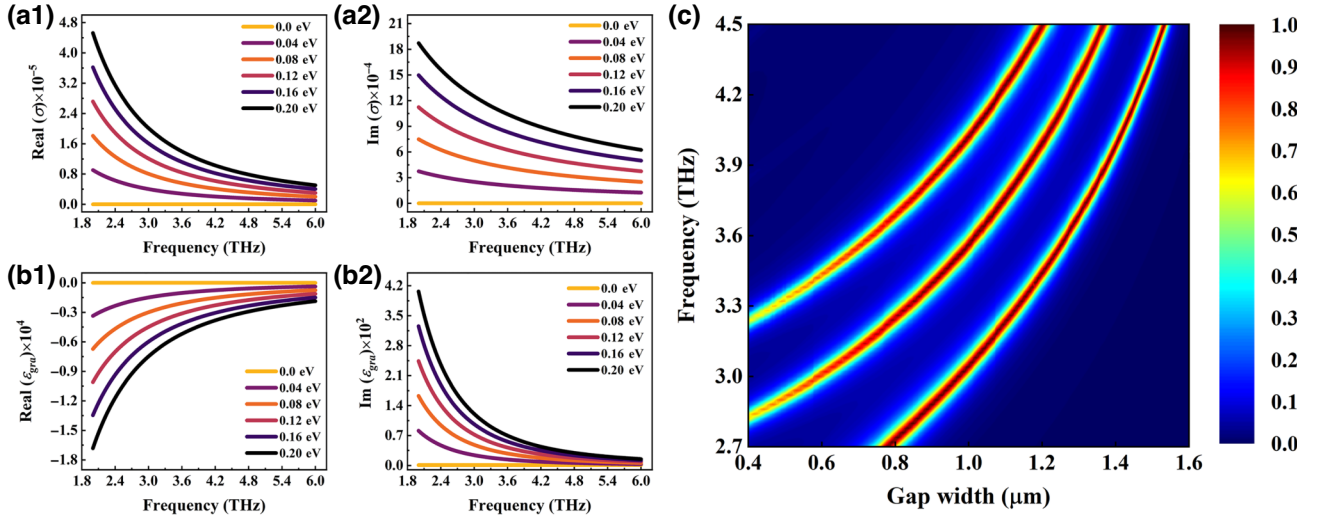


FIG. 2. (a1) Real part and (a2) imaginary part of graphene conductivity. (b1) Real part and (b2) imaginary part of graphene relative permittivity. (c) Relationship between absorptance, frequency, and gap width with a constant period of 6 μm .

reported by using atomic force microscopy, ranging from 0.34 to 1.7 nm [50]. Additionally, the effective wavelength of the localized surface-plasmon polaritons (LSP) excited by the incident THz wave is longer than the thickness of monolayer graphene. Considering both of the above factors, the thickness of monolayer graphene is set to 1 nm [14,31] to simplify the calculation. The width, W_{gra} , of the graphene strips and the gap, W_{gap} , between the graphene strips are both 1 μm , and the period, P , is 6 μm . Compared with the wavelength of the incident THz wave, ranging from 66.67 to 111.11 μm (the corresponding frequency ranges from 2.7 to 4.5 THz). Therefore, the graphene strips and the gaps cannot be distinguished by the incident THz wave due to the subwavelength-structure effect. Nevertheless, for the excited LSP on the graphene surface, the resonance peak can be tuned over a wide range due to the reduction of the graphene strip width, as shown in Fig. 2(c).

The incident plane wave is set as TM polarized (p polarized) with a magnetic field intensity of $H_0 = 1$ A/m and power of $P_{\text{in}} = 1$ W/m. After determining the above boundary conditions and material parameters, the electromagnetic wave frequency-domain solver is implemented to solve the wave equation. Then, the electromagnetic field distribution map can be obtained directly, and the absorption spectrum can be calculated via $A(\omega) = 1 - R(\omega) - T(\omega)$, where $R(\omega) = |S_{11}|^2$ and $T(\omega) = |S_{21}|^2$ are the reflectance and transmittance, respectively. S_{11} and S_{21} are the reflection and transmission coefficients, respectively.

III. RESULTS AND DISCUSSION

A. A universal method of realizing multiband perfect absorber

Although considerable progress has been made in developing multiband perfect absorbers consisting of a

graphene-based metasurface, challenges of complex manufacturing and the requirement for numerous processing steps in previous investigations have prevented further advancement. To address these drawbacks, a universal method of creating a multiband perfect absorber is proposed. Unlike previous research with identical Fermi levels for each graphene metasurface unit, in this work, to generate multiband absorption, several metasurface units are combined into a large period and multiple Fermi levels are applied to the various units inside the expanded period.

In the following, single-band and dual-band absorbers are realized to demonstrate the validity of our proposal. A model of the device and the Fermi-level distribution are built and shown in Figs. 3(a1) and 3(b1). For the single-band mode, all the metasurface units have the same Fermi level of 0.088 eV (E_{F1}) with a period of 2 μm . A notable resonance peak exists in Fig. 3(a2) with the absorptance of 98.8% at 2.89 THz. The inset shows the intensity distribution of the electric field mainly concentrated at both edges of the graphene strip. In Fig. 3(b1), the dual-band mode is depicted with two Fermi levels added to a larger metasurface period, causing the corresponding period to increase to 4 μm , which is twice that of the single-band mode. The Fermi levels of the left and right metasurface are found at 0.088 eV (E_{F1}) and 0.118 eV (E_{F2}), correspondingly. The absorption spectrum in Fig. 3(b2) shows two distinct peaks, one to the left of 99.3% at 2.99 THz and the other to the right of 97.1% at 3.58 THz. Furthermore, the triple-band mode is also obtained in Sec. III B. The left inset demonstrates that the left absorption peak depends on the left resonance mode caused by the graphene unit at 0.088 eV. The same happens on the right side. These results and analyses demonstrate the effectiveness of the proposed method

of achieving multiband absorption. Therefore, according to the approach of introducing multiple resonance modes (Fermi levels) into an expanded period, the arbitrary multiband perfect absorber can be realized. Compared to previous multiband devices, which have complex patterned graphene (such as a ring structure with eight T-shaped graphene strips [28] or a double regular hexagon with ten T-shaped strips [29]) or a multilayer structure (such as double-stacked nanodisk and nanohole graphene [26], dual-layer ring, and rectangular strip [32]), the proposed absorber possesses the obvious advantage of a concise pattern and structure.

The tunable performance, which is the most important capability of graphene, is also studied here. For the single-band mode, Fig. 3(a3) exhibits the absorptance as a function of incident frequency from 2.7 to 4.5 THz and Fermi level from 0.045 to 0.185 eV. As a result, the resonant frequency can be tuned over a wide range from 2.7 to 4.2 THz. For the dual-band mode, by setting both Fermi levels, maintaining $E_{F1} = 0.088$ eV and scanning E_{F2} from 0.045 to 0.185 eV, the result is shown in Fig. 3(b2). It should be noted that, when E_{F2} is 0.088 eV, two resonance peaks merge, since the two resonance modes are equivalent. Hence, based on the premise that the absorber's physical structure remains the same, switching between single-band and dual-band modes can be quickly accomplished by adjusting the Fermi level.

B. Arbitrary switching from n -band to m -band modes with a digital coding metasurface

In Sec. III A, an innovative approach to realize a multiband perfect absorber is displayed. However, to achieve the switching of dual-band and triple-band modes, the design idea shown in Fig. 3(b1) is ineffective. Once the metal wiring is completed, the dual-band mode cannot be converted into triple-band modes, and three resonance modes are not allowed to exist in an expanded period with merely two metasurface units. Similarly, the single-band mode of Fig. 3(a1) is not able to switch to dual-band or triple-band modes.

To obtain a more flexible type of switching of absorption modes, a THz arbitrarily switchable perfect absorber from n -band to m -band modes with a digital coding metasurface is designed, as shown in Fig. 4(a). Since we aim to realize arbitrary mode conversion within three bands, the proposed absorber possesses eight working modes, as listed in Table I, namely, 1 zero-band mode, 3 single-band modes, 3 dual-band modes, and 1 triple-band mode. The corresponding absorption spectrums are presented in Figs. 4(b), 4(c1)–4(c3), 4(d1)–4(d3), and 4(e). For instance, Fermi levels E_{F1} , E_{F2} , and E_{F3} for the 110 mode are 0.088, 0.118, and 0 eV, respectively. The absorption spectrum is shown in Fig. 4(d1) with a newly expanded period of $6 \mu\text{m}$, which is different from the dual-band mode shown in Fig. 3(b2) with a period of $4 \mu\text{m}$. The absorptances at

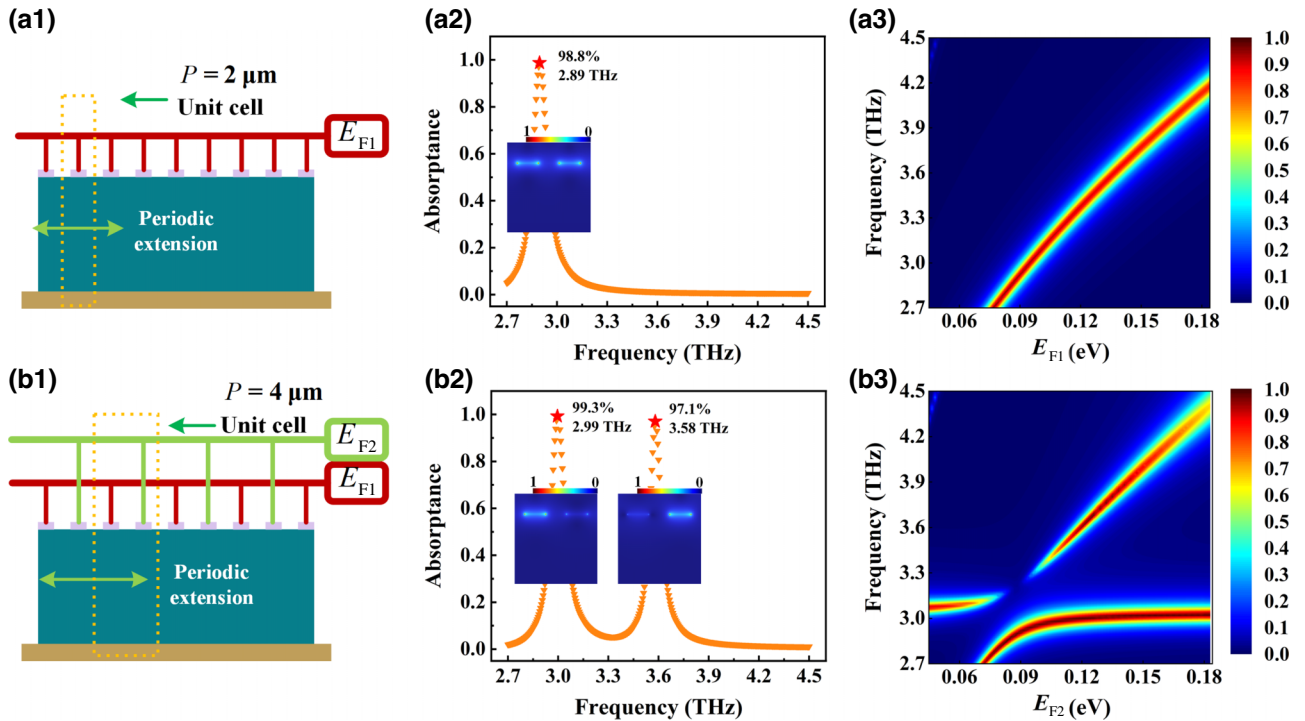


FIG. 3. Profile (a1),(b1) and absorption spectrum (a2),(b2) of a perfect absorber for single-band and dual-band modes. (a3),(b3) Absorptance as a function of incident frequency and Fermi level. (a3) Changing E_{F1} without E_{F2} . (b3) Changing E_{F2} , maintaining $E_{F1} = 0.088$ eV.

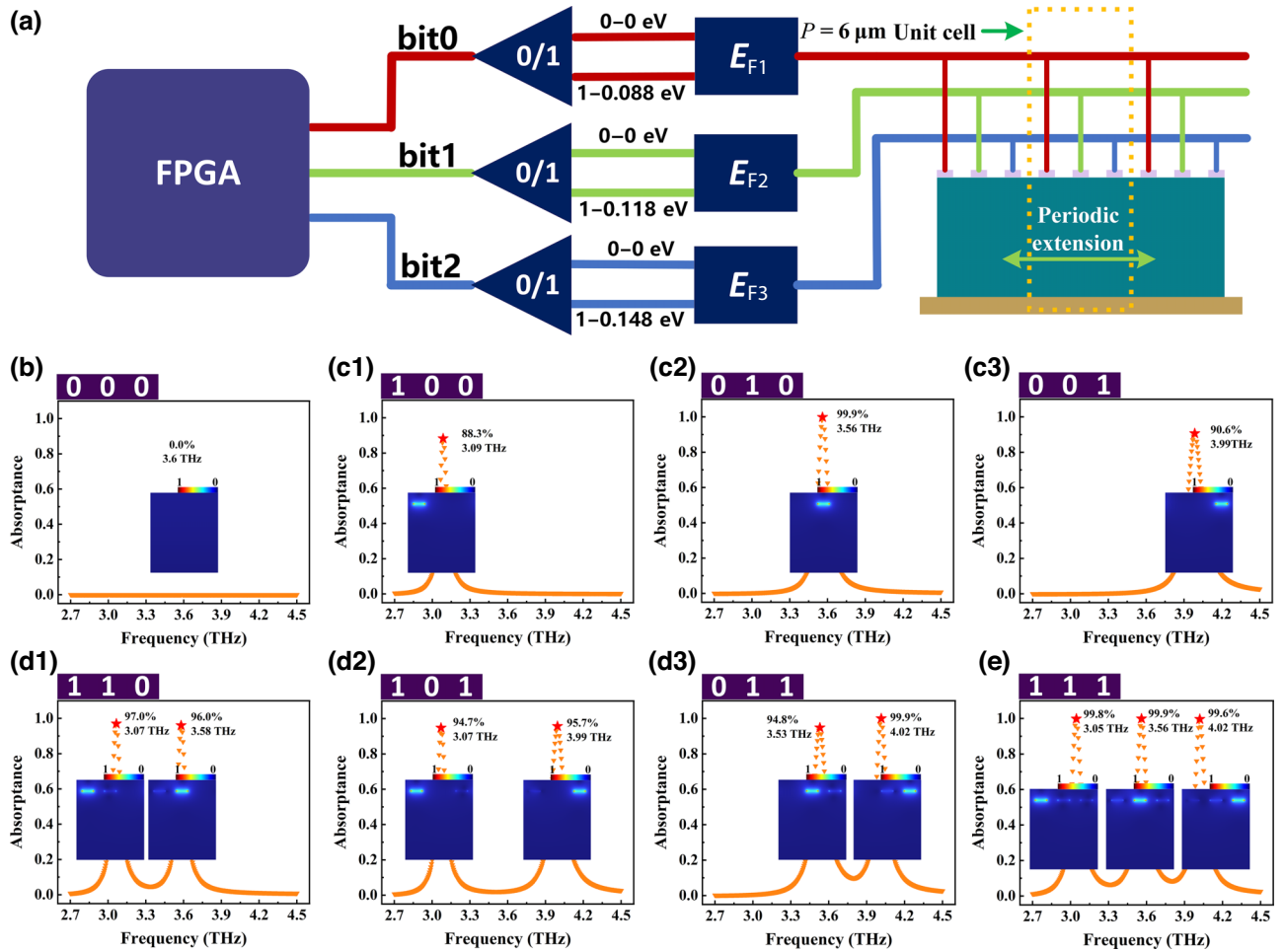


FIG. 4. (a) Schematic diagram of a digital coding metasurface with eight different modes through FPGA programming. (b) Absorption spectrum of 000 zero-band coding mode. (c1)–(c3) Absorption spectra of 100, 010, and 001 single-band coding modes. (d1)–(d3) Absorption spectra of 110, 101, and 011 dual-band coding modes. (e) Absorption spectrum of 111 triple-band coding mode.

3.07 and 3.58 THz are 97% and 96%, respectively. The absorption spectrum of the 111 mode with Fermi levels of 0.088, 0.118, and 0.148 eV is apparent in Fig. 4(e) with absorptances of 99.8%, 99.9%, and 99.6% at 3.05, 3.56, and 4.02 THz, respectively.

As a consequence, the arbitrary mode conversion of the n band and m band can be easily accomplished using

TABLE I. Working modes of digital coding perfect absorber.

Absorption mode	Coding mode	E_{F1} (eV)	E_{F2} (eV)	E_{F3} (eV)
Zero band	000	0	0	0
Single band	100	0.088	0	0
	010	0	0.118	0
	001	0	0	0.148
Dual band	110	0.088	0.118	0
	101	0.088	0	0.148
	011	0	0.118	0.148
Triple band	111	0.088	0.118	0.148

FPGA digital programming. Particularly, the absorptance for the 000 mode always remains zero, and the incident electromagnetic wave is completely reflected. This is because the relative permittivity of graphene is proportional to the conductivity, which is in a direct ratio to the Fermi level. While E_{F1} , E_{F2} , and E_{F3} are entirely equal to zero, the real part of relative permittivity is one, and the imaginary part vanishes. Since graphene is currently equal to air, there is no absorptance and loss. Hence, it is simple to implement absorption-mode conversion between the n band and m band using digital programming in FPGA. Additionally, the newly formed larger metasurface period must contain n Fermi levels. The above description and analysis confirm that the proposed digital coding metasurface offers numerous absorption modes and more flexible switching capabilities in contrast to published research, which merely has one absorption mode and cannot achieve multiband conversion.

To explicitly illustrate the intrinsic mechanism of the perfect absorber, impedance-matching theory is used in the

following analysis. The absorptance can be expressed as

$$A = 1 - R = 1 - \left| \frac{Z - Z_0}{Z + Z_0} \right|^2 = 1 - \left| \frac{Z_r - 1}{Z_r + 1} \right|^2, \quad (5)$$

$$Z_r = \sqrt{\frac{(1 + S_{11})^2 - S_{21}^2}{(1 - S_{11})^2 - S_{21}^2}}, \quad (6)$$

where R is the reflectance, Z is the effective impedance of the integral structure, and Z_0 is the impedance of free space with a real part of one and an imaginary part of zero. $Z_r = Z/Z_0$ represents the relative impedance. S_{21} is equal to zero as the bottom metal prevents the propagation of the transmission wave.

Figures 5(b1)–5(b3) present the real part and imaginary part of the relative impedance at the 010 single-band, 110 dual-band, and 111 triple-band modes, respectively. The yellow solid lines indicate the positions of the resonance peaks corresponding to those of Figs. 5(a1)–5(a3), where the real parts of relative impedance are close to one and the imaginary parts almost approach zero. This demonstrates that the impedance of the proposed absorber matches that of free space, so the reflectance of the absorber reaches zero and the power of the incident wave is completely absorbed. The absorptance (99.8%, 99.9%, and 99.6%) of the three resonance peaks for the 111 mode is larger than that of the 110 mode (97% and 96%). Compared to the imaginary part (0.05, 0.06, 0.12) of the three resonance peaks for the 111 mode, the imaginary part (0.19, 0.38)

of the two resonance peaks for the 110 mode is larger and farther away from the imaginary part 0 of Z_0 . Similarly, the real part (0.68, 0.92) of the relative impedance of the 110 mode is smaller than that of the 111 mode (0.93, 0.96, 1.0) and farther away from the real part 1 of Z_0 . These results reveal that there is better impedance matching with air for the 111 mode than the 110 mode. Additionally, the real and imaginary parts of the relative impedance can provide more important information about the physical properties of multiband perfect absorption. As shown in Figs. 5(a1)–5(a3), the resonance peaks obtained from the S parameters have a small right shift compared to the maximum absorption value obtained from the impedance's real part, as shown in Figs. 5(b1)–5(b3). This can be well understood by considering the dispersion contribution from the imaginary part of the impedance. That is, the position of the resonant absorption peaks displayed by the S parameter is determined by both the real and imaginary parts of the impedance.

In the proposed THz multiband perfect absorber, an FP cavity is designed to enhance the resonance absorption effect of THz waves, which is formed between the graphene strips and the bottom metal. On one hand, to prove the existence of the FP cavity, the thickness of diamond varies from 0.1 to 100 μm , and the incident frequency ranges from 2.7 to 5.7 THz. Figure 6(a1) shows a significant periodic resonance peak that occurs with the variation of diamond thickness, indicating the presence of an FP cavity. Meanwhile, an interesting phenomenon

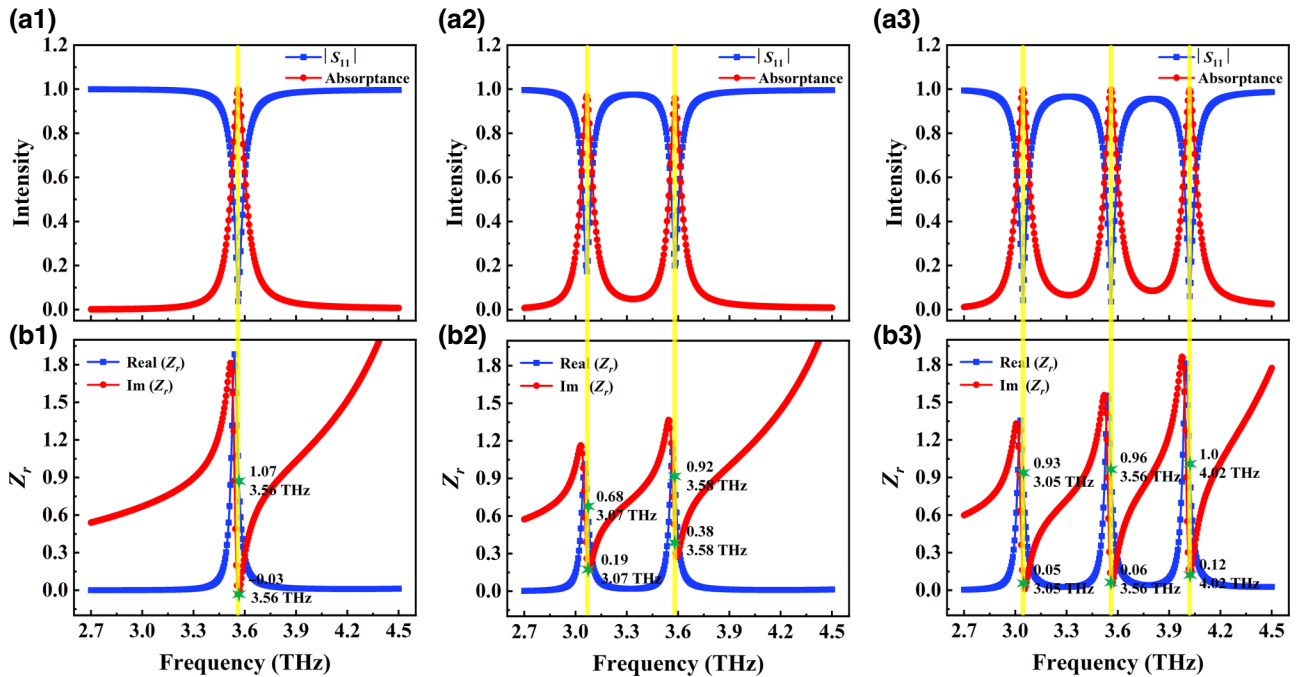


FIG. 5 (a1)–(a3) S_{11} , absorptance, and (b1)–(b3) real and imaginary parts of the relative impedance for 010 single-band, 110 dual-band, and 111 triple-band modes at resonance peaks, respectively.

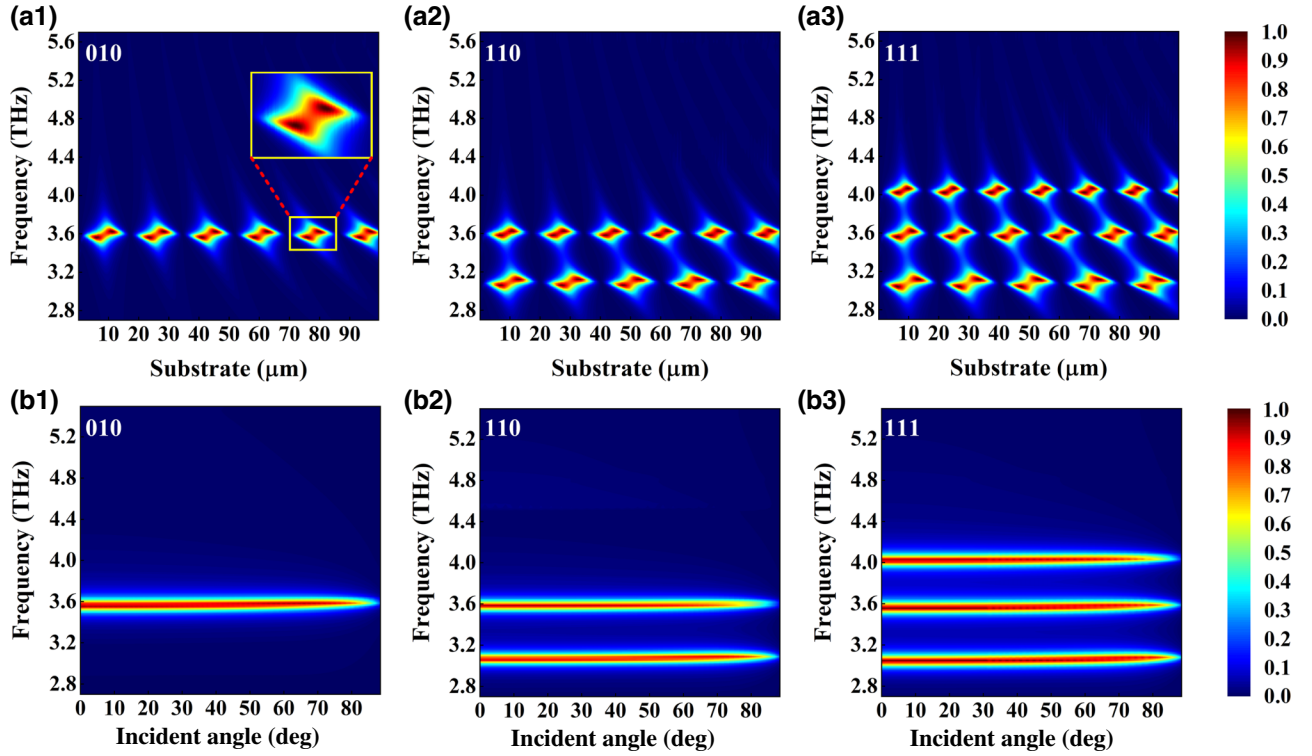


FIG. 6. Absorption as a function of incident frequency and (a1)–(a3) substrate thickness or (b1)–(b3) incident angle for 010 single-band, 110 dual-band, and 111 triple-band modes of the absorber.

was observed by scanning the diamond thickness, namely, Rabi splitting, which is formed by the strong coupling interaction between the FP resonance of graphene strips and local intrinsic modes, as shown in the illustration in Fig. 6(a1). According to the dressed-state theory [51], the resonant frequency of the FP cavity varies with the length of the cavity, and the length of the cavity is tuned if the thickness of the diamond substrate changes, which leads to crossing being avoided and a significant Rabi splitting. On the other hand, by changing the thickness of diamond, the optimal geometric parameters can be provided for the implementation of future absorption devices, and the optimal diamond thickness obtained here is 6.1 μm for the 010, 110, and 111 absorption modes in Figs. 6(a1)–6(a3), respectively.

To assess the robustness of the perfect absorber, this section focuses on how different incident angles affect absorptance. We define the angle of incident light vertical to the absorber surface as zero angle (0°). For the 010 single-band mode, the influence of incident frequency and angle on absorption is shown in Fig. 6(b1). The absorber retains 90% absorptance over 0° – 55° at 3.56 THz. Figures 6(b2) and 6(b3) depict the absorptance distribution for the 110 dual-band and 111 triple-band modes. Concerning the absorption spectrum of all the resonance peaks, it still maintains more than 90% absorptance at an incident angle of 55° . Consequently, the proposed perfect absorber

for all the resonance modes possesses great angle tolerance and good robustness.

IV. CONCLUSION

A universal method of realizing a multiband perfect absorber in the THz regime is demonstrated through introducing multiple different Fermi levels into an expanded period. Results reveal that nearly 99% perfect absorption can be realized for the single-band, dual-band, and triple-band modes. It is found that the resonant peaks can be dynamically tuned by the Fermi level. Eight states are generated by the digital coding metasurface under FPGA control, namely, zero-band (000), single-band (100, 010, 001), dual-band (110, 101, 011), and triple-band (111) modes. The random switching between n -band and m -band modes can be conducted through digital programming. The real part and imaginary part of the relative impedance indicate that the perfect absorption is attributed to perfect impedance matching with the free space. Furthermore, the absorbers consistently exhibit perfect absorption in the 010, 110, and 111 modes at a dielectric thickness of 6.1 μm . Through scanning the incident angle, we find that the absorber possesses great angle tolerance and robustness, while maintaining an absorptance over 90% with an incident angle of 50° . The proposed absorber is dynamically switchable and tunable by adjusting the Fermi level.

Hence, it may find potential applications in THz switchable filters, sensors, and 6G communication.

ACKNOWLEDGMENTS

This work was supported by the National Natural Science Foundation of China (Grants No. 62074127, No. U21A2073, No. 61804122, No. 11874142, No. 61627812, No. 61705176, No. 11874102, No. 11474048, and No. 61805068), the Natural Science Foundation of Shaanxi Province (Grants No. 2018JQ6002, No. 2021JQ062, No. 2021JQ056, and No. 2021GY223), the Postdoctoral Science Foundation (Grants No. 2019M653637, No. 2019M660256, and No. 2017M620300), the National Key Research and Development Program of China (Grant No. 2018YFE0125900), the Fundamental Research Funds for the Central Universities (Grant No. ZYGX2019J102), the National Key R&D Program of China (Grants No. 2017YFB0402800 and No. 2017YFB0402802), and the Natural Science Basic Research Program of Shaanxi (Program No. 2024JC-YBMS-505)

The idea for the manuscript came from S.Z. and F.W., and the writing was mainly completed by S.Z. Other authors participated in the discussion of the results. All authors have accepted responsibility for the entire content of this manuscript and approved its submission.

The authors declare no conflicts of interest.

-
- [1] M. Hasan, S. Arezoomandan, H. Condori, and B. Sensale-Rodriguez, Graphene terahertz devices for communications applications, *Nano Commun. Netw.* **10**, 68 (2016).
- [2] M. Chen, L. Singh, N. Xu, R. Singh, W. Zhang, and L. Xie, Terahertz sensing of highly absorptive water-methanol mixtures with multiple resonances in metamaterials, *Opt. Express* **25**, 14089 (2017).
- [3] M. Gezimati and G. Singh, *Advances in Terahertz Technology for Cancer Detection Applications* (Springer, US, 2023), pp. 55.
- [4] X. Ruan, X. Ruan, and H. Huang, Application of terahertz spectroscopy in medical microbiological detection, *J. Phys.: Conf. Ser.* **2425**, 012045 (2022).
- [5] M. Gezimati and G. Singh, Terahertz cancer imaging and sensing: Open research challenges and opportunities, *Opt. Quantum Electron.* **55**, 1 (2023).
- [6] F. Wen, H. Ye, X. Zhang, W. Wang, S. Li, H. Wang, Y. Zhang, and C. Qiu, Optically induced atomic lattice with tunable near-field and far-field diffraction patterns, *Photonics Res.* **5**, 676 (2017).
- [7] F. Wen, X. Zhang, H. Ye, W. Wang, H. Wang, Y. Zhang, Z. Dai, and C. W. Qiu, Efficient and tunable photoinduced honeycomb lattice in an atomic ensemble, *Laser Photonics Rev.* **12**, 1 (2018).
- [8] F. Wen, S. Hui, S. Zhang, Z. Wu, Z. Liu, T. Zhu, F. Lin, W. Wang, Y. Zhang, and H. Wang, Tunable continuous-variable tripartite entanglement via cascaded third-order nonlinear processes in a ring cavity, *Ann. Phys.* **534**, 1 (2022).
- [9] J. B. Pendry, A. J. Holden, D. J. Robbins, and W. J. Stewart, Magnetism from conductors and enhanced nonlinear phenomena, *IEEE Trans. Microw. Theory Tech.* **47**, 2075 (1999).
- [10] Z. Liu, G. Hu, H. Ye, M. Wei, Z. Guo, K. Chen, C. Liu, B. Tang, and G. Zhou, Mold-free self-assembled scalable microlens arrays with ultrasmooth surface and record-high resolution, *Light: Sci. Appl.* **12**, 143 (2023).
- [11] N. I. Landy, S. Sajuyigbe, J. J. Mock, D. R. Smith, and W. J. Padilla, Perfect metamaterial absorber, *Phys. Rev. Lett.* **100**, 1 (2008).
- [12] H. Tao, C. M. Bingham, D. Pilon, K. Fan, A. C. Strikwerda, D. Shrekenhamer, W. J. Padilla, X. Zhang, and R. D. Averitt, A dual band terahertz metamaterial absorber, *J. Phys. D: Appl. Phys.* **43**, 225102 (2010).
- [13] A. S. Arezoomand, F. B. Zarrabi, S. Heydari, and N. P. Gandji, Independent polarization and multi-band THz absorber base on Jerusalem cross, *Opt. Commun.* **352**, 121 (2015).
- [14] R. Alaei, M. Farhat, C. Rockstuhl, and F. Lederer, A perfect absorber made of a graphene micro-ribbon metamaterial, *Opt. Express* **20**, 28017 (2012).
- [15] Y. Zhang, Y. Feng, B. Zhu, J. Zhao, and T. Jiang, Graphene based tunable metamaterial absorber and polarization modulation in terahertz frequency, *Opt. Express* **22**, 22743 (2014).
- [16] L. Wang, S. Ge, W. Hu, M. Nakajima, and Y. Lu, Graphene-assisted high-efficiency liquid crystal tunable terahertz metamaterial absorber, *Opt. Express* **25**, 23873 (2017).
- [17] X. Wang, G. Wu, Y. Wang, and J. Liu, Terahertz broadband adjustable absorber based on VO₂ multiple ring structure, *Appl. Sci.* **13**, 252 (2023).
- [18] W. Chen, C. Li, D. Wang, W. An, S. Gao, C. Zhang, and S. Guo, Tunable wideband-narrowband switchable absorber based on vanadium dioxide and graphene, *Opt. Express* **30**, 41328 (2022).
- [19] H. Li and J. Yu, Bifunctional terahertz absorber with a tunable and switchable property between broadband and dual-band, *Opt. Express* **28**, 25225 (2020).
- [20] M. Jiang, Z. Song, and Q. H. Liu, Ultra-broadband wide-angle terahertz absorber realized by a doped silicon metamaterial, *Opt. Commun.* **471**, 125835 (2020).
- [21] J. Liu, P. Li, Y. Chen, X. Song, Q. Mao, Y. Wu, F. Qi, B. Zheng, J. He, H. Yang, *et al.*, Flexible terahertz modulator based on coplanar-gate graphene field-effect transistor structure, *Opt. Lett.* **41**, 816 (2016).
- [22] F. Wen, S. Zhang, S. Hui, H. Ma, S. Wang, H. Ye, W. Wang, T. Zhu, Y. Zhang, and H. Wang, Terahertz tunable optically induced lattice in the magnetized monolayer graphene, *Opt. Express* **30**, 2852 (2022).
- [23] A. C. Tasolamprou, A. D. Koulouklidis, C. Daskalaki, C. P. Mavidis, G. Kenanakis, G. Deligeorgis, Z. Viskadourakis, P. Kuzhir, S. Tzortzakis, M. Kafesaki, *et al.*, Experimental demonstration of ultrafast THz modulation in a graphene-based thin film absorber through negative photoinduced conductivity, *ACS Photonics* **6**, 720 (2019).
- [24] H. Li, L. Wang, and X. Zhai, Tunable graphene-based mid-infrared plasmonic wide-angle narrowband perfect absorber, *Sci. Rep.* **6**, 1 (2016).

- [25] G. Yao, F. Ling, J. Yue, C. Luo, J. Ji, and J. Yao, Dual-band tunable perfect metamaterial absorber in the THz range, *Opt. Express* **24**, 1518 (2016).
- [26] P. Sun, C. You, A. Mahigir, T. Liu, F. Xia, W. Kong, G. Veronis, J. P. Dowling, L. Dong, and M. Yun, Graphene-based dual-band independently tunable infrared absorber, *Nanoscale* **10**, 15564 (2018).
- [27] D. Wu, M. Wang, H. Feng, Z. Xu, Y. Liu, F. Xia, K. Zhang, W. Kong, L. Dong, and M. Yun, Independently tunable perfect absorber based on the plasmonic in double-layer graphene structure, *Carbon* **155**, 618 (2019).
- [28] K.-D. Xu, J. Li, A. Zhang, and Q. Chen, Tunable multi-band terahertz absorber using a single-layer square graphene ring structure with T-shaped graphene strips, *Opt. Express* **28**, 11482 (2020).
- [29] M. Darvishi Bahloli, A. Bordbar, R. Basiri, and S. Jam, A tunable multi-band absorber based on graphene metasurface in terahertz band, *Opt. Quantum Electron.* **54**, 1 (2022).
- [30] Z. Ding, W. Su, H. Lu, H. Wu, and H. Yao, Terahertz absorber based on double-layer graphene metasurface with tunable absorption window and intensity, *Opt. Laser Technol.* **163**, 109446 (2023).
- [31] X. Tang, H. Jia, L. Liu, M. Li, D. Wu, K. Zhou, P. Li, L. Tian, D. Yang, and W. Wang, A tunable terahertz absorber based on double-layer patterned graphene metamaterials, *Materials (Basel)* **16**, 4166 (2023).
- [32] P. Zamzam, P. Rezaei, and S. A. Khatami, Quad-band polarization-insensitive metamaterial perfect absorber based on bilayer graphene metasurface, *Phys. E* **128**, 114621 (2021).
- [33] J. Huang, J. Li, Y. Yang, J. Li, J. Li, Y. Zhang, and J. Yao, Broadband terahertz absorber with a flexible, reconfigurable performance based on hybrid-patterned vanadium dioxide metasurfaces, *Opt. Express* **28**, 17832 (2020).
- [34] Y. Liu, R. Huang, and Z. Ouyang, Terahertz absorber with dynamically switchable Dual-Broadband based on a hybrid metamaterial with vanadium dioxide and graphene, *Opt. Express* **29**, 20839 (2021).
- [35] J. Ge, Y. Zhang, H. Dong, and L. Zhang, Nanolayered VO₂-based switchable terahertz metasurfaces as near-perfect absorbers and antireflection coatings, *ACS Appl. Nano Mater.* **5**, 5569 (2022).
- [36] Z. Zhan, J. Wei, Y. Miao, and Q. Wang, Polarization-independent narrowband terahertz filter based on all-dielectric metasurfaces, *IEEE Photonics J.* **15**, 1 (2023).
- [37] D. Liu, X. Yu, F. Wu, W. Du, L. Chen, F. Liu, M. Kuwahara, and S. Ono, Terahertz high- Q quasi-bound states in the continuum in laser-fabricated metallic double-slit arrays, *Opt. Express* **29**, 24779 (2021).
- [38] D. Liu, X. Yu, F. Wu, W. Du, L. Chen, F. Liu, M. Kuwahara, and S. Ono, Terahertz asymmetric metallic hole arrays with polarization-independent quasi-bound states in the continuum for membrane sensing, *Opt. Express* **31**, 23608 (2023).
- [39] G. Kwon, Y. H. Choi, H. Lee, H. S. Kim, J. Jeong, K. Jeong, M. Baik, H. Kwon, J. Ahn, E. Lee, *et al.*, Interaction- and defect-free van der Waals contacts between metals and two-dimensional semiconductors, *Nat. Electron.* **5**, 241 (2022).
- [40] S. Zhao and K. Larsson, First principle study of the attachment of graphene onto different terminated diamond (111) surfaces, *Adv. Condens. Matter Phys.* **2019**, 8 (2019).
- [41] Y. Ma, Y. Dai, M. Guo, and B. Huang, Graphene-diamond interface: Gap opening and electronic spin injection, *Phys. Rev. B* **85**, 1 (2012).
- [42] P. Németh, K. Mccoll, R. L. Smith, M. Murri, L. A. J. Garvie, M. Alvaro, B. Pécz, A. P. Jones, F. Corà, C. G. Salzmänn, *et al.*, Diamond-graphene composite nanostructures, *Nano Lett.* **20**, 3611 (2020).
- [43] N. Tokuda, M. Fukui, T. Makino, D. Takeuchi, S. Yamasaki, and T. Inokuma, Formation of graphene-on-diamond structure by graphitization of atomically flat diamond (111) surface, *Jpn. J. Appl. Phys.* **52**, 110121 (2013).
- [44] G. Giovannetti, P. A. Khomyakov, G. Brocks, V. M. Karpan, J. Van Den Brink, and P. J. Kelly, Doping graphene with metal contacts, *Phys. Rev. Lett.* **101**, 4 (2008).
- [45] S. Peng, Z. Jin, D. Zhang, J. Shi, Y. Zhang, and G. Yu, Evidence of electric field-tunable tunneling probability in graphene and metal contact, *Nanoscale* **9**, 9520 (2017).
- [46] P. Dore, A. Nucara, D. Cannavò, G. De Marzi, P. Calvani, A. Marcelli, R. S. Sussmann, A. J. Whitehead, C. N. Dodge, A. J. Krehan, *et al.*, Infrared properties of chemical-vapor deposition polycrystalline diamond windows, *Appl. Opt.* **37**, 5731 (1998).
- [47] T. Ruf, M. Cardona, C. S. J. Pickles, and R. Sussmann, Temperature dependence of the refractive index of diamond up to 925 K, *Phys. Rev. B* **62**, 16578 (2000).
- [48] G. Partridge, G. Lu, P. May, and J. W. Steeds, Potential high-strength high thermal conductivity metal-matrix composites based on diamond fibres, *Diam. Relat. Mater.* **4**, 848 (1995).
- [49] L. Ye, Y. Chen, G. Cai, N. Liu, J. Zhu, Z. Song, and Q. H. Liu, Broadband absorber with periodically sinusoidally-patterned graphene layer in terahertz range, *Opt. Express* **25**, 11223 (2017).
- [50] P. Nemes-Incze, Z. Osváth, K. Kamarás, and L. P. Biró, Anomalies in thickness measurements of graphene and few layer graphite crystals by tapping mode atomic force microscopy, *Carbon* **46**, 1435 (2008).
- [51] P. Anisimov and O. Kocharovskaya, Decaying-dressed-state analysis of a coherently driven three-level system, *J. Mod. Opt.* **55**, 3159 (2008).